Author's Accepted Version of the following paper:
Shweiki, S., Rezayat, A., Tamarozzi, T., Mundo, D., Transmission Error and strain analysis of lightweight gears by using a hybrid FE-analytical gear contact model, Mechanical Systems and Signal Processing, Volume 123, 15 May 2019, Pages 573-590
https://doi.org/10.1016/j.ymssp.2019.01.024

Transmission Error and Strain Analysis of Lightweight Gears by using a Hybrid FE-Analytical Gear Contact Model

Shadi Shweiki[1 2], Ali Rezayat[2], Tommaso Tamarozzi[2 3] and Domenico Mundo[1]

[1] *Department of Mechanical, Energy and Managment Engineering, University of Calabria, Italy* {*shadi.shweiki,domenico.mundo*}*@unical.it*
[2] *Siemens Industry Software NV, Leuven, Belgium* {*ali.rezayat,tommaso.tamarozzi*}*@siemens.com*
[3] *Department of Mechanical Engineering, Katholieke Universiteit Leuven, Belgium*

Abstract — *In this paper the transmission error and the strain field are analysed for two gear pairs, with different lightweight designs, reflecting the common industrial practice. The methodology used for the analysis is based on a hybrid FE-Analytical approach implemented in a multibody solver which allows to achieve a good accuracy with a low computational effort. The specific formulation allows to well describe the deformation field of the gear body from which the strain values can be computed at specific locations in the FE model. The numerical method used in this work is validated both in terms of transmission error and strain field, using the results obtained from an experimental campaign performed on a high-precision gear test rig.*

Keywords — Multibody simulations, Contact mechanics, Gear contact, Transmission error, Stress recovery, Experimental validation.

1 Introduction

Geared mechanical transmissions are some of the most common subsystems in many fields of the mechanical industry, from the more established ones, such as heavy equipments, wind turbines and precision machinery to relatively new areas represented by robotics and electric vehicles. Generally in all these applications the transmission is one of the most expensive components and a potential substitution cost or maintenance time can be very high. Taking as reference the wind energy industry according to [1], in a typical wind turbine, the gearbox is recognized to be the component with the second lowest failure rate, but on the other side it is responsible for up to 40% of the total downtime, being the repairing time the longest compared to all the components. The study of gears behaviour, especially for fault prevention and prediction where cracks, pitting, mounting and manufacturing errors cause additional excitations, still involves the attention of the researchers [2], [3] and represents an actual research topic [4], [5] also in condition monitoring applications [6].
Additionally, new and more demanding environmental regulations enforce different design targets focused on the global efficiency of the system in order to reduce greenhouse gas emissions and fuel consumption especially in the automotive and aerospace industries. One of the possible strategies to cope with such constraints is a reduction of the mass of each component of the system. Different approaches to achieve this goal in geared transmissions are currently under research. For instance in [7], the dynamic performance of gear bodies manufactured using composite materials is evaluated. More established approaches to reduce the weight are based on the manufacturing of gears with thin bodies, possibly with holes and slots. These approaches however impact on the dynamic behaviour of the gears [8] increasing the global compliance of the gear pair and generating higher and more complex stress field in sensitive parts of the gear body. According to [9], excessive load in different regions of the gear causes typical failure modes, such as pitting on the tooth surface or crack propagation on the tooth root. In [10] the importance of

the root stress as design parameter is empathised by its inclusion in the constraints of an optimisation strategy for the design of cylindrical involute gears. When lightweight gears are used the complex shape of the gear body adds multiple regions where stress concentrations may occur. The accurate simulation of the meshing process without any limitation on the body shape is therefore fundamental for the evaluation of strength criteria in the gear body and to perform durability analyses in lightweight gears.
Due to the complexity of the gear meshing process, accurate simulation tools are needed to provide the required level of detail. Non linear Finite Element (FE) analyses are able to provide the highest level of accuracy, especially when contact load distribution on the tooth surface is investigated [11]. One of the drawbacks is that the computational time is particularly high, limiting the use of such tools to static analyses or to very short dynamic events at component level. The time required to simulate even short time-domain phenomena of few milliseconds is still prohibitively large with standard FE solutions. In the work of Ziegler and Eberhard [12], FE simulations are used as reference and in one of the case studies reported the time required to simulate 13 impacts between two gears for a total duration of 300 ms is about 194 hours on a standard machine. The reason for the high computational efforts required by FE simulations is in the high number of degrees of freedom required to properly model the contact area. Other approaches different from the full FE discretization are investigated by other authors. In [13] a combination between FE formulation together with an analytical description of the local contact displacement is used to address the problem of simulating the gear under meshing conditions. An extension of the method is used for the analysis of a gear pair [14] and of a planetary gear set [15] under dynamic conditions but this method still has limited applicability for time-domain simulations at system-level. The same approach is used to compare the time-domain strain in external gears [16] and in planetary gear stages [17], but the analysis was not extended to lightweight gears.
Multibody (MB) simulation tools are often used to simulate the behaviour of a complete transmission, under the assumption that the meshing gears can be represented as rigid bodies connected to each other by spring-damper elements. By exploiting the much lower computational cost with respect to FE-based methods, MB approaches allow to simulate longer events. However, accurate results are achievable only if the position-dependent mesh stiffness is properly modelled [18]. Although MB simulation tools are extensively used to investigate the dynamic behaviour of geared transmissions because of the low computational cost, their application in the study of lightweight gear meshing as well as in stress and strain analyses is limited, since the detailed elastic deformation field of the gear body is not available in most of the implementations. Using elastic MB formulations the displacement field is available for the recovery of stress and strain in the components either online during the time integrations or offline in a post-processing phase [19] with an obvious increase of the simulation time compared to rigid MB simulations. Model order reduction techniques can be used to improve the efficiency of the simulation: in [20] the problem of recovering the stress field in MB gear simulation is analysed using different model reduction techniques.
In this work an elastic MB approach combining FE and analytical representations of the gear stiffness contributions is used to investigate the meshing behaviour of lightweight gears [21] where different blank geometries are designed to reduce the overall mass of the transmission. The advanced elastic MB formulation provides an higher computational efficiency when compared to state-of-the-art elastic MB approaches, allowing at the same time to precisely describe the gear mesh stiffness and to recover the strain field in the gear body of lightweight gears. Section 2 describes the hybrid FE-analytical gear contact model used to enable a time-varying representation of the mesh stiffness in the MB simulation environment. The methodology for stress recovery and strain field estimation is illustrated in section 3. Several experiments have been conducted in order to evaluate the robustness of the proposed technique. This methodology has been validated using the data obtained from different experimental campaigns, using the in-house gear test rig. In particular the transmission error and stress values have been acquired and compared to the corresponding simulated signals. Two gear sets with different body geometries have been analysed. The detailed analysis of the results is presented in section 4.

2 Gear Contact Model

This paper investigates the behaviour of two gear pairs, in which a standard cylindrical gear engages with a ligthweight gear using an elastic MB formulation based on the combination of the FE method and an analytical representation. The main motivation behind the application of the methodology is a reduction of the computational

requirements typical of the non linear FE approach used in gear simulations, while ensuring an accurate description of the gear meshing process that is verified by comparing the simulation results with experimental measurements. The approach used in this work is based on a penalty formulation of the contact problem [22], where in an initial contact detection phase, the unphysical penetration between the meshing teeth is computed according to the relative position of the gears and to the actual working conditions. In a second step the contact loads are computed based on the penetration between the meshing teeth and a contact stiffness. The potential teeth in contact are searched exploiting the kinematics equations of meshing defined by the tooth geometry and spatial position of the gear [23] [24]. The assumption behind the contact detection phase is that the deformation of the gear profile remains small, so that the contact points are considered to lie on a rigid involute profile in the direction defined by the normal to the unmodified tooth flank. No a-priori assumptions are made on the global displacement of the gears in the reference frame, while the deformation under load of different components, such as flexible shafts and cases, bushings and bearings, may change the relative position of the gears with respect to the initial one.
The above assumption does not represent a limit for most of the industrial applications where metallic gears are used, with a tooth profile that is nearly the theoretical one. When gears with a deviation from the perfect involute geometry (i.e. gears with micro-modifications) are analysed, the amount of deviation is generally very slight and the geometrical definition of the profile normals is only marginally affected by the modifications, so that the difference between the actual and the theoretical position of the normal direction to the tooth surface is negligible. The changes in the contact point position due to the micro-modifications, instead, are taken into account. These assumptions may lose their applicability when extremely low stiffness materials are used for the gears (e.g. rubber-like materials), but this does not represent the focus of this work.
The penetration between the meshing teeth and the relative velocities of the tooth, which represent the output of the contact detection phase, are computed for each active tooth pair (i.e. meshing teeth) using a slicing approach, where the teeth are divided into multiple slices along the width, under the assumption that these quantities remain constant along the width of each segment. The slicing approach used in the contact detection phase improves the accuracy of the solution and is particularly relevant in the case of misaligned gears or profile modifications along the tooth width, where the load distribution along the tooth width may be non-uniform. The subdivision of the tooth width in different slices enables a finer discretization of the tooth surface. The advantage is that the penetration is computed for each slice of the contacting tooth pairs. The importance of the approach is relevant when misaligned gears or gears with lead modifications are considered. For example, in the case of spur gears with angular misalignment, one side of the tooth can not even touch the corresponding region of the paired tooth on the other gear, while the other side may exhibit a huge amount of penetration. If the slicing approach is not implemented, an average value of penetration is calculated and the real load distribution along the tooth thickness is neglected.
As result of the contact detection phase a set of penetration values between the tooth profiles for each segment is available and can be used as input for the subsequent force calculation phase. The tooth stiffness computation reflects the teeth slicing approach where a stiffness vector is computed for each segment of the engaged teeth of the two meshing gears, i.e. gear *1* and gear *2*. The stiffness vector has a dimension which depends on the number of the considered slices, being the coupling terms between the slices included in the formulation. For each loaded slice, the coupling terms are computed from the displacements of the nodes belonging to the other slices of the tooth. Similarly to what was described for the contact detection phase, the inclusion of the coupling terms results in a more accurate estimation of the meshing stiffness. The coupling terms, in fact, allow to fill the stiffness matrix with off-diagonal elements, which improves the estimated load distribution along the tooth thickness. In the case of lightweight gears, where the thin body generates a mesh stiffness which is highly variable along the width of the tooth, the inclusion of the coupling terms is essential for an accurate analysis of contact phenomena.
The mathematical description of the force computation phase is provided by equations 1, 2 and 3 in the form of a non-linear complementarity problem (NLCP) [25], which is solved at each time step of the time domain simulation for each active slice:

$$\begin{aligned} \boldsymbol{\Delta}^{12} - f(\mathbf{F_n}^{12}, geom_{12}, E_{12}, \nu_{12}) + \\ +[\boldsymbol{C}^1(geom_1, E_1, \nu_1 + \boldsymbol{C}^2(geom_2, E_2, \nu_2)]\ \mathbf{F_n}^{12} = \\ = \mathbf{g}(\mathbf{F_n}^{12}, geom_{12}, E_{12}, \nu_{12}) \geqslant 0 \end{aligned} \tag{1}$$

$$\mathbf{F_n}^{12} \geqslant 0 \tag{2}$$

$$\mathbf{g}(\mathbf{F_n}^{12}, geom_{12}, E_{12}, \nu_{12})^{\mathrm{T}} \cdot \mathbf{F_n}^{12} = 0 \tag{3}$$

where:

- Δ^{12} is the vector of instantaneous penetrations on each active slice for each of the teeth that are simultaneously in contact at a certain time instant. The penetration vector is corrected for the contribution due to the micro geometry in the normal direction;
- $\mathbf{F_n}^{12}$ is the vector of unknown contact forces in the normal direction with respect to the involute profile;
- $\mathbf{f}(\mathbf{F_n}^{12}, geom_{12}, E_{12}, \nu_{12})$ is a vector of non-linear functions of the normal contact forces that accounts for the non-linear Hertzian contact compliance effects. The terms $geom_{12}, E_{12}, \nu_{12}$ represent known input parameters related to the gears geometry and material properties;
- $\boldsymbol{C}^i(geom_{\mathrm{i}}, E_{\mathrm{i}}, \nu_{\mathrm{i}})$ is a full matrix that includes the FE based compliance for gear i;
- $\mathbf{g}(\mathbf{F_n}^{12}, geom_{12}, E_{12}, \nu_{12})$ is the penetration.

From the structure of eq. 1, it can be noted that the total displacement field of each gear is computed starting from a decomposition of the stiffness data into two contributions, which is the main assumption on which the approach is based. The description of the main concept of the method can be found in [26] where the idea of the decomposition of the gear meshing stiffness is developed, but its application is limited to static analyses. An extension of the method to the study of the dynamic behaviour of helical gear pairs can be found in the work of Andersson [27]. In [28] the approach is exploited in a flexible MB formulation showing an improvement of the computational performances compared to state-of-the-art flexible MB approaches, without showing a relevant reduction in the accuracy. A schematic representation of the decomposition of the gear displacement field is shown in figure 1:

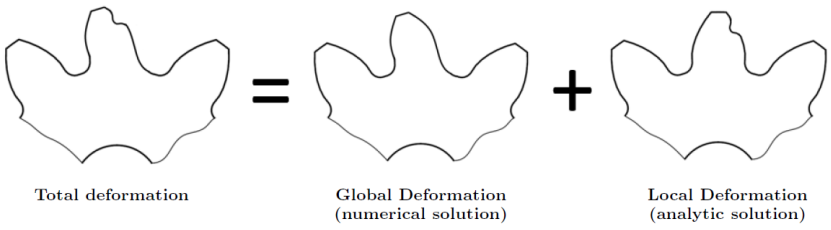

Fig. 1: Decomposition of the gear displacement field in meshing conditions, [28]

Therefore the total deformation of the gear resulting from the meshing process is considered as the superposition of two different contributions:

- **A global linear deformation** caused by the tooth bending and shear as well as by complex effects due to the gear body geometry and coupling between different teeth (e.g. when one tooth is loaded, also adjacent teeth will deform.
- **A local non-linear deformation** represented by the terms caused by locally non-linear Hertzian-like effects;

The first contribution representing the global deformation, is the response of the gear to tooth bending and shear loads originated during the meshing, coupled with the complex effects due to the topology of the gear body and with the coupling between different teeth. The displacement field of gear i (with i=1,2,n), considered as linear, can be modelled using a linear FE approach. The resulting stiffness matrix $\boldsymbol{K}_{FE}{}^{i}$ is build with a relatively coarse mesh compared to the one used in the contact analyses with non-linear FE formulations. This is possible since the non-linear contact phenomena are not taken into account while computing the linear component of the displacement field.
The geometrical properties of the problem of two meshing gears allow to exploit the symmetry in order to further increase the computational efficiency of the problem. When two gears engage only a few teeth pairs are loaded simultaneously, while the others are unloaded. This means that a small set of nodes are loaded in the FE stiffness matrix of the gear $\boldsymbol{K}_{\mathrm{FE}} \in \mathbb{R}^{n_{FE} \times n_{FE}}$ (where n_{FE} is the number of degrees of freedom of the FE model of the gear), while all the other nodes belonging to the un-engaged teeth as well as to the gear body are unloaded. The dimension of the problem can be therefore reduced by the use of a reduction space to condense the information contained in the FE stiffness matrix, according to equation 4, resulting in a reduced stiffness matrix $\boldsymbol{K}_{red}{}^{i} \in \mathbb{R}^{n_C \times n_C}$:

$$\boldsymbol{K}_{red}{}^{i} = \boldsymbol{\Psi}^{\mathrm{i}\mathrm{T}} \boldsymbol{K}_{\mathrm{FE}}{}^{\mathrm{i}} \boldsymbol{\Psi}^{\mathrm{i}} \tag{4}$$

In this work, the used reduction space $\boldsymbol{\Psi}^{\mathrm{i}} \in \mathbb{R}^{n_{FE} \times n_C}$ is obtained by the concatenation of n_C deformation patterns. Each pattern is computed based on a procedure similar to the one detailed in [26], which allows to condense the contact analysis into a smaller problem. By following this approach, the model still keeps an accuracy comparable with the one of the original FE model when the latter is subject to meshing loads.
Each of the n_C deformation patterns, representing the global deformation field of the gear, is the result of a linear static simulation with a normal load applied on each of the chosen nC flank nodes belonging to a potential contacting surface.
As previously explained, the reduced stiffness matrix $\boldsymbol{K}_{red}{}^{i}$ has to model only the global deformation field of the gears. Each of the deformation patterns in the reduction space is therefore computed according to the scheme represented in figure 2, where the first two images on the right-side refer to the FE-based calculations. In the same figure, the rightmost image represents the analytical non-linear contact deformation. The number of deformation patterns, and consequently of the n_C loaded nodes, depends on the number of nodes in the FE model and on the number of slices in which each tooth is divided. Both parameters can be defined by the user.

Fig. 2: Computational steps to represent gear total deformation [28]. The brown lines correspond to the constrained surface in the FE simulations.

The global deformation field of the gear computed using the FE method is performed in two computational steps, as shown in figure 2. In the first step, the actual static deformation of the gear after the application of a point load in the normal direction, to one node belonging to the tooth surface is calculated, while the nodes corresponding to the internal hub surface are constrained. This step however includes also the unphysical local effects due to the point load application on the FE mesh. The latter contribution must be removed since it partially contains a local effect that, in the proposed approach, is modelled using the analytical representation instead. The effects of the local Hertzian contribution are not included in the global deformation of the gears and hence must be removed. The local effect can be removed by superimposing an additional deformation field obtained applying a point load in the opposite direction on the loaded tooth while the nodes belonging to the opposite external surface of the tooth

are costrained, as can be shown in figure 2.
It is noteworthy that the FE formulation allows to represent the global deformation of the gears implicitly considering all the different combinations of tooth and body shapes, including the detailed effects arising from the holes and thinned bodies that are typical in lightweight gears. The formulation used exploits these consideration in order to compute the contact forces in a numerically efficient manner. The numerical results obtained using this methodology are compared with the experimental ones in section 4.
Friction effects are modelled in the MB approach following a regularized Coulomb model. The friction force $\mathbf{F_t}^i$ for the $i-th$ slice is computed after the computation of the elastic force $\mathbf{F_n}^i$ as proportional to the latter by the friction coefficient:

$$\mathbf{F_t}^i = \mu \mathbf{F_n}^i \tag{5}$$

The computation is performed for each slice of the engaged tooth pairs, according to eq. 5. The friction force is applied in the tangential direction to the tooth flank. Particular attention is given to the determination of the instant where the contact point crosses the pitch point, causing a reversal in the direction of the friction force acting on a given slice.

3 Stress recovery

The problem of dynamic stress recovery in gear simulations has already been investigated by other authors using different techniques. In order to obtain a detailed description of the strain or stress fields in the gears under meshing conditions the displacement field in the elastic gear body has to be available. Different formulations are used in literature to model the compliance of gear, making the displacement field of the gear bodies available. In the work of Cooley [29] an analytical representation of the gear body flexibility is used to analyse the gyroscopic effects in the frequency response of high-speed transmissions where the gear body compliance is fundamental in determining its dynamic behaviour. The formulation used is based on the analytical elastic equation of curved beams and rings. However analytical representations have limited applicability to specific applications and provide poor accuracy when gears with complex body shapes are considered, which is the case of gears with a lightweight design. An FE discretization of the gears enables a high level of accuracy of the computed displacement field without any assumption on the geometry of the gear body, but on the other hand the size of the problem is considerably increased.
In the study of [30] a modal reduced model is used, allowing to drastically reduce the computational time compared to non-linear transient FE simulations. In another work [12] the approach is extended to a multibody environment using a floating frame of reference formulation to perform impact analysis on very compliant gear with a lightweight design. The results in terms of strains are also validated with experimental results. The analyses however are limited to impact simulations between a gear and another body with a total duration of a few milliseconds, while longer events, covering several meshing cycles are not analysed.
The problem of reducing the size of the model is also faced in [31] using a different approach based on a parametric model order reduction scheme. In that work, numerical results are used as reference for the validation of the stress field. The application of this scheme to elastic MB simulation of gear meshing can be found in [32] where a good agreement with the FE results, taken as reference, is shown. The analysis however is still limited to short-time events, and moreover the effects of a lightweight design on the meshing behaviour are not analysed.
The transient elastic MB analysis of lightweight meshing gears in relatively long events (compared to impact analysis) is addressed in this work. The simulation results, including the strain analysis are validated using experimental data.
For this purpose, the strain value at a specific location $\boldsymbol{r}(x,y,z)$ and at a given simulation time t can be computed in a post processing phase once the displacement field $\mathbf{d}^i(\mathbf{r},t) \in \mathbb{R}^{n_{FE}\times 1}$ of gear i is available, using the formulation of eq. 6.

$$\epsilon(\mathbf{r},t) = \boldsymbol{B}\ \boldsymbol{dn}^i(\mathbf{r},t) = \begin{bmatrix} \frac{\partial}{\partial x} & 0 & 0 \\ 0 & \frac{\partial}{\partial y} & 0 \\ 0 & 0 & \frac{\partial}{\partial z} \\ \frac{\partial}{\partial y} & \frac{\partial}{\partial x} & 0 \\ \frac{\partial}{\partial z} & 0 & \frac{\partial}{\partial x} \\ 0 & \frac{\partial}{\partial z} & \frac{\partial}{\partial y} \end{bmatrix} \boldsymbol{dn}^i(\mathbf{r},t) \tag{6}$$

Where the matrix $\boldsymbol{dn}^i(\mathbf{r},t) \in \mathbb{R}^{3\times n_{nodeFE}}$, being n_{nodeFE} the number of nodes in the FE model, is the matrix form of the nodal displacements contained in $\mathbf{d}^i(\mathbf{r},t)$. Different scenarios are open when the displacement field $\mathbf{d}^i(\mathbf{r},t)$ in the gear body i is recovered from the MB simulation and its mathematical description is related to the elastic MB formulation used to solve the gear meshing process. In this paper two different techniques, corresponding to two different representations of the displacement field are used to recover the strain field in the post-processing phase.

1. In the first of the suggested approaches the nodal displacement field vector $\mathbf{d}^i(\mathbf{r},t)$ is computed according to eq. 7:

$$\mathbf{d}^i(\mathbf{r},t) = \boldsymbol{\Psi}^{\mathbf{i}}(\mathbf{r})\ \mathbf{q}^i(t) \tag{7}$$

where the matrix $\boldsymbol{\Psi}^{\mathbf{i}}(\mathbf{r})$ is the column matrix representing the reduction space of eq. 4 for the *i-th* gear and it is formed by concatenating the n_C static modes. The symbol $\mathbf{q}^{\mathbf{i}}(t) \in \mathbb{R}^{n_C\times 1}$ represents the vector of the modal participation factors, that can be computed online during the MB simulation, by projecting the physical forces $\mathbf{F_n}^i$ on the global reduction space for the gear i and solving the reduce problem by using the reduced stiffness matrix.
It is important to note that the modal participation factors set $\mathbf{q}^{\mathbf{i}}(t)$ of gear i are functions of the simulation time and each of them is the output of a single time step of the multibody simulation, therefore the displacement computation has to be repeated for each time frame of the simulation.

2. In the second approach the displacement field $\mathbf{d}^i(\mathbf{r},t)$ is computed by solving eq. 8, where $\boldsymbol{K}_{\mathrm{FE}}$ is the full FE stiffness matrix of the gear and $\mathbf{F}^i_{FE}(\mathbf{r},t) \in \mathbb{R}^{n_{FE}\times 1}$ is the vector of the nodal loads. The vector $\mathbf{F}^i_{FE}$ is not directly available after the MB simulation. According to eq. 1, at each timestep, only the vector $\mathbf{F}^i_n$ is available. The latter contains all the meshing loads $\mathbf{F}^i_e$ acting on each slice e for all the meshing teeth.

$$\mathbf{d}^i(\mathbf{r},t) = {\boldsymbol{K}^i_{FE}}^{-1}\mathbf{F}^i_{FE}(\mathbf{r},t) \tag{8}$$

All the forces $\mathbf{F}^i_e$ are placed at the centre of each slice in which the tooth width is divided, and therefore can not be guaranteed to be located exactly in the nodes of the corresponding FE model. The latter, corresponding to the force acting on each slice, consists in a load applied in known positions on the tooth flank. For each load $\mathbf{F}^i_e$ a corresponding finite element is individuated in the FE mesh. At this point, by knowing the position of the application point of the force $\mathbf{F}^i_e$ and the nodal coordinates of the corresponding loaded element it is possible to compute the nodal distribution, and therefore, to assemble the entire nodal loads vector. Based on the assumed shape functions in the FE formulation, the vector of nodal loads $\mathbf{F}^i_{FE}(\mathbf{r},t)$ can therefore be retrieved by computing the element nodal load vector $\mathbf{s}^i_e \in \mathbb{R}^{(node_{el}\times 3)\times 1}$ containing the nodal distribution of a concentrated load acting on the element for each loaded element e of the *i-th* gear. In this context $node_{el}$ represents the number of nodes for each element, depending on the chosen formulation. Each vector $\mathbf{s}^i_e$ can be computed from the vector of the three-dimensional meshing loads $\mathbf{F}^i_e$ acting on each

slice e of the tooth surfaces exploiting the relation in eq. 9 [33], where $\boldsymbol{N}_e^i$ is the shape functions matrix of the *e-th* element computed at the application point of the *e-th* meshing force of gear i. It has to be noted that each force $\mathbf{F}_e^i$ acting on a slice, contained in the vector $\mathbf{F}_n^i$, corresponds to a force applied on the corresponding e element in the FE mesh.

$$\mathbf{s}_e^i = \boldsymbol{N}_e^{iT} \mathbf{F}_e^i \qquad \text{where } \boldsymbol{N}_e^i \in \mathbb{R}^{3\times(node_{el}\times 3)} \tag{9}$$

Each shape functions depends on the natural coordinates of the meshing force application point $\mathbf{x}_e^i \in \mathbb{R}^{3\times 1}$ on the external face of the element. The shape function matrix is therefore a non-linear function of the natural coordinates. Once the application point of the meshing force $\mathbf{F}_e^i$ in the global reference frame at a given timestep is known from the time-domain simulation, its value can be used to find the shape functions contained in $\boldsymbol{N}_e^i$ by solving equations 10:

$$\mathbf{x}_e^i - \mathbf{P}_e^i = 0 \qquad\qquad \mathbf{P}_e^i = \boldsymbol{N}_e^i \, \mathbf{x}_{ne}^i \tag{10}$$

Where $\mathbf{P}_e^i \in \mathbb{R}^{3\times 1}$ is the position of the *e-th* contact point of gear i defined using the isoparametric formulation. The vector $\mathbf{x}_{ne}^i \in \mathbb{R}^{(node_{el}\times 3)\times 1}$ represents the spatial coordinates of the *e-th* element nodes in the deformed state defined in the same reference frame as $\mathbf{x}_e^i$.
It has to be noted that the vector of the meshing loads Fe is given in the global reference frame, in which the gears are represented as rigid bodies. In the strain recovery phase, the gears are kept fixed, and the load is considered to move. However, the angular position of the gears is available from the MB simulation. This makes it possible to rotate the meshing loads and apply them in the proper location and in a direction that is normal to the tooth profile.

4 Experimental Validation

The numerical results obtained by applying the methodology presented in this work to the analysis of lightweight gears have been validated using multiple experimental results in terms of strain at the tooth root as well as of TE, which is an important quantity when the performance of a geared transmission are considered.
The importance of the TE arises from its consideration as one of the main excitation sources in a system where meshing gears are present [34]. It can be defined as the difference between the actual position of the driven gear and the position it would occupy if the gears were infinitely rigid and the tooth profiles perfectly conjugate.
Clearly a relative displacement is present if two meshing gears are not perfectly rigid or if their flanks are not perfectly conjugate (e.g. with ideal involute profiles). This relative displacement overlaps the pure kinematical one, and its amplitude is determined by different phenomena:

1. The geometrical contribution is present when two micro-modified gears are meshing. Their relative rotation is not anymore the pure kinematical motion resulting from a couple of perfect involute gears. The micro modifications result in a geometrical effect that can be determined based on the teeth surface geometry.

2. The tooth and gear body contribution arises from the deformations due to the applied load and is highly dependent on the geometry of the gear teeth, and gear body and the actual working conditions of the gears.

3. The local non-linear contact deformation is a contribution arising from the contacting tooth surfaces. The contact pressure distribution generates a Hertzian type displacement field, which is non-linear with the applied load. It is mostly not dependent on the gear body geometry, but depends on tooth shape and material;

In conventional, non-lightweight gears, the TE curves are typically dominated by the harmonic content at the meshing frequency originated mainly from the gear deformation in the tooth region. One of the effects of gear lightweighting is the occurrence of additional harmonic components at lower frequencies, originating from the nonuniform distribution of material along the gear blank caused by the holes, which generates an additional nonuniform deformation in the gear body. In this work the TE is computed according to the following expression:

$$TE = r_{\mathrm{bG}}\theta_{\mathrm{G}} - r_{\mathrm{bP}}\theta_{\mathrm{P}} \tag{11}$$

where θ_{G} and θ_{P} represent the rotation of the gear and of the pinion, respectively, while r_{bG} and r_{bP} are their base radii. Therefore the angular relative displacement of the gears is converted into a linear motion along the line of action.

4.1 Numerical models and test-cases

In this paper, three spur gears are tested arranged into two gear pairs, each of them consisting of one standard gear and one gear in which a lightweight design is machined. The standard gear presents also a profile modification of 10 microns. The latter is intentionally applied on the gear with the two goals of making the meshing process smoother by reducing the edge contact effects at higher loads and also to validate the capabilities of the methodology to properly model the geometrical contribution of tooth micro-modifications to the TE. The geometrical specifications and the micro-modifications, consisting of profile crowning centred on the operating pitch diameter of 150mm, are summarized in Table 1.

Tab. 1: Main design parameters of the analysed gears

Parameter	**Units**	**Gear 1**	**Gear 2**	**Gear 3**
Tooth number	[-]	57	57	57
Pressure angle	[deg]	20	20	20
Module	[mm]	2.6	2.6	2.6
Face width	[mm]	23	23	23
Micromodifications	[μm]	10 (profile crowning)	-	-
Lightweighting	[-]	-	thin rimmed	thin rimmed & 3 slots
Web thickness	[mm]	-	5	5
Rim diameter	[mm]	-	136.7	136.7

A CAD representation of the analysed gear pairs is reported in figure 3, where the different body topology of the gears can be observed. In the gear pair of figure 3a gear 1 and gear 2 are meshing. Gear 2 presents a lightweight design in which the mass reduction is obtained by an axis symmetrical material removal, resulting in a thin-rimmed gear. In this case, the TE is dominated by the tooth bending under load and by the high body compliance of the gear.

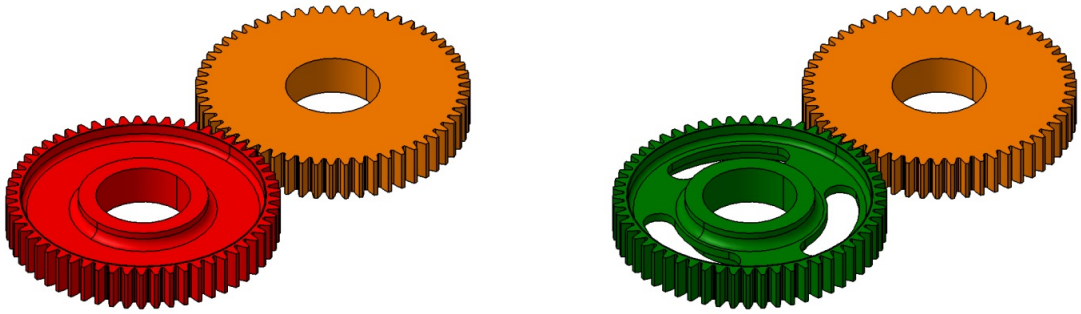

(a) Gear pair A (b) Gear pair B

Fig. 3: CAD representation of the two gear pairs analysed.

A second case-study, consisting of the gear pair B represented in figure 3b, is also analysed. In such a case, the solid gear 1 engages with gear 3. The latter has an extremely lightweight design, achieved by three slots machined in the thin body of the gear.

4.2 Experimental setup

The experimental activities were performed using the high precision gear testrig [35], that is shown in figure 4. The test-rig allows to measure different physical quantities in meshing gears, in both static and dynamic conditions, for different working conditions in terms of applied load, relative displacements of the gears and shaft compliance. In this work the focus is on the TE and on the strain levels measured in different location of the gear under multiple load conditions.

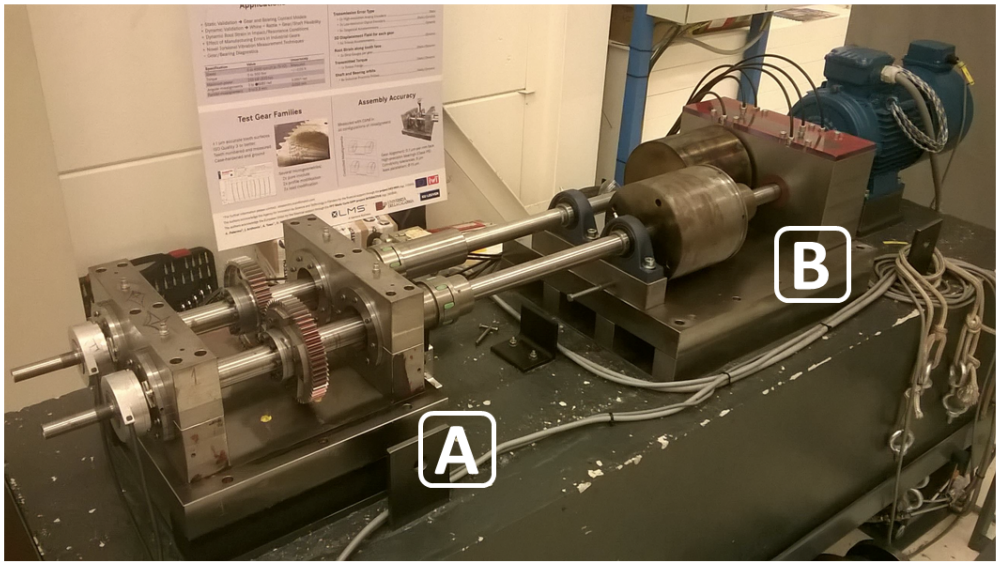

Fig. 4: A picture of the test rig right. It is possible to distinguish the test side on the left (A), where the test gears are placed. The reaction side is located on the right (B).

The test-rig has a power circulation arrangement, in which two main subsystems can be identified: the test side and the reaction side. These parts are dynamically separated from each other by using flexible couplings. The tested gears are mounted at the test side, while the other gear pair is not intended to be instrumented and its utility lies

in reacting the applied torque on test gears. One of the advantages of this arrangement is that the torque required to spin the shaft is relatively low, being just the torque needed to overcome the friction forces acting between the meshing teeth and inside the bearings. This simplifies the application of smooth speed and constant torque pre-loads and facilitates the measurement of rotational and linear vibrations in the system.
During the tests performed in this work the gears were rotated at a low rotational speed of about 10 rpm, in order to properly measure the static contribution to the mesh stiffness fluctuation to the TE.
Due to the small amplitude of the quantities measured in the campaign, the gears were manufactured with tight tolerances and measured tooth by tooth in the profile and lead directions. Tooth surfaces have been hardened and precision ground to ISO quality 3 (equivalent to AGMA 15). The relatively uncommon geometrical parameters of the gears were chosen in order to decrease the tooth stiffness, as to emphasize the signal-to-noise ratio of the measured TE and of strain values. The resulting teeth geometry allows also the mounting of strain gauges at the tooth root.

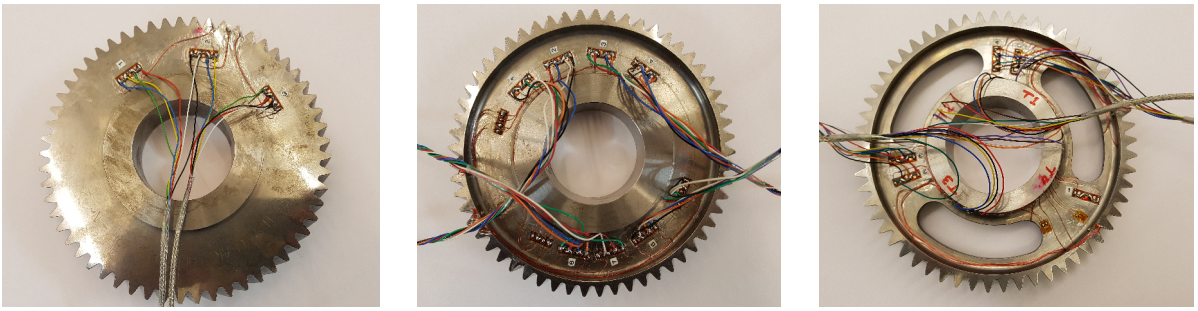

(a) Gear1: standard design (b) Gear 2: lightweight design, thin body. (c) Gear 3: lightweight design, three slots.

Fig. 5: Picture of the gears used in the experimental campaign.

A figure of the gears used in the experimental campaign is shown in 5, where it is possible to notice the different lightweight designs of the gear body. The gears were instrumented at several locations to allow accurate measurements of the strain levels. Figure 6 gives a detailed picture of a strain gauge applied on the tooth root of a gear. Every strain gauge has been connected to an independent full bridge circuit, also attached to the gear body. As the full bridge connections are located on the rotating components, a slip-ring is necessary to transfer the measured strain signals to the data acquisition device. Preliminary experimental results showed that the signal-to-noise ratio of the measured strain signals are improved in comparison to the case where quarter bridge is applied. The slip rings mounted on both rotating shafts make it possible to accurately measure the dynamic strain signals in different speed conditions.

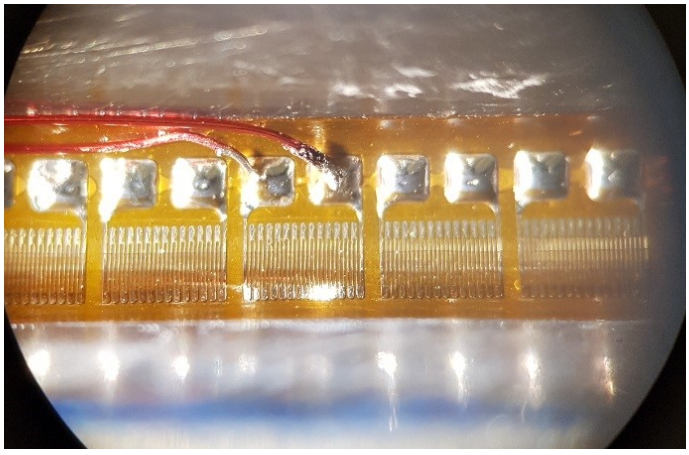

Fig. 6: A magnified view of the strain gages attached to the tooth root area (intermediate stage).

In the measurement campaign, the raw data has been acquired by a SCADAS frontend sampling at 51.2 kHz for a time duration of 60 s. The rotating angle of each gear was accurately measured using ERN 120 digital encoders, installed on corresponding shafts. These optical encoders provide 5000 pulses per revolution, which is largely sufficient for the purpose of the test campaign. In addition, a tacho pulse signal was emitted by each encoder once a complete shaft revolution was achieved. The raw strain signals have been acquired through rotating Wheatstone circuits with full bridge configuration (attached to the gears) to increase the signal-to-noise ratio of the strain signals. Once the measurements were conducted, the acquired raw data was post-processed in order to extract the vibration characteristics of the gears in each test case. The post-processing procedure is summarized as follows. The raw data (measured in time domain) is converted to angle domain; where the measured tacho signals coming from both encoders allow to divide the TE signal into corresponding shaft revolutions. The TE data of each revolution is converted to order domain using the Fourier transform and the spectra corresponding to the different shaft revolutions are averaged together in order domain. The obtained spectra is then filtered to remove the order 0 and 1 corresponding to the mean value and to the contribution given by the eccentricity of the gear on the shafts. The latter is removed since this effect is not taken into account in the simulation model. Finally, the obtained spectra is converted back to angle domain using the inverse Fourier transform.

4.3 Transmission Error Validation

In this section the results in term of TE are reported for both the analysed gear pairs. The comparison between the measured and the simulated transmission error for gear pair A is shown in figure 7, where the different curves are reported in angle domain to remove the effect of speed fluctuations intrinsically present in the experimental data sets. The experiments were conducted for different torque levels, ranging from 50 to 300Nm, while the rotational speed was kept low at around 10 rpm in order to exclude any dynamic effects from this validation process. Due to the low rotational speed, a relatively high friction coefficient equal to 0.3 was chosen for the simulations. Such a choice can be justified by the consideration that for low rotational speed a consistent lubricant film can not be developed between the flanks of the meshing teeth.
The comparison between the measurements and the simulated results for all the applied torque values shows that the proposed method is capable to properly model the geometrical non-linearities present due to the contact loads. The coupling between the increased compliance coming from the lightweight design and the stiffness variations due to the changes in the instantaneous number of meshing tooth pair at high loads is also well represented.
At low loads the mesh stiffness fluctuation is smoother and the good correlation achieved proves that the contact detection algorithm is capable of modelling the geometrical components of the TE generated by the microgeometry modifications with a high level of accuracy.

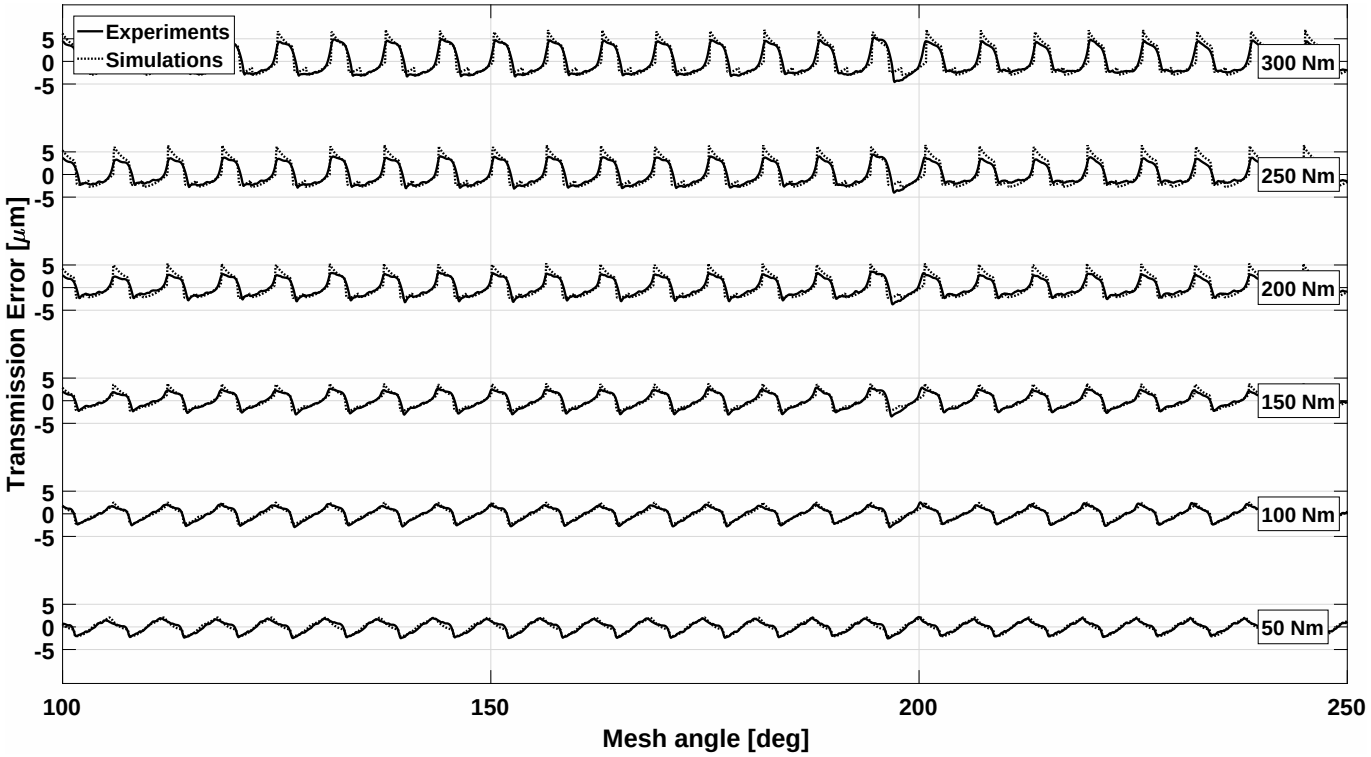

Fig. 7: Transmission error in angle domain for different torque for gear pair A.

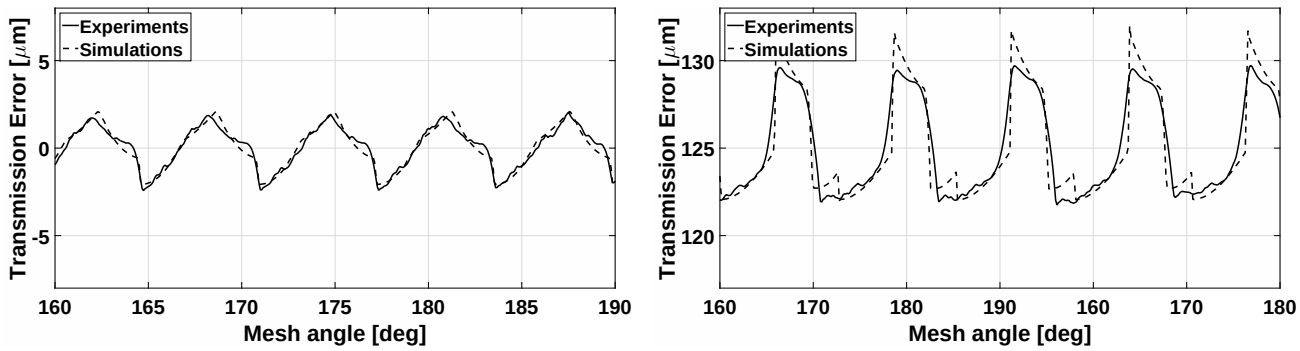

(a) 50 Nm

(b) 300 Nm

Fig. 8: Detail of the transmission error in angle domain for gear pair A for different torque levels.

In figure 8, it is interesting to see how both measurements and simulations show the same particular shape of TE, which is dominated by the microgeometry in the first case (figure 8a) and by the high friction forces in the second case (figure 8b). In the latter case, sharp TE variations can be appreciated, due to the friction reversal phenomena occurring after each angular pitch in the position along the meshing cycle where, the relative speed between the tooth profiles changes sign.

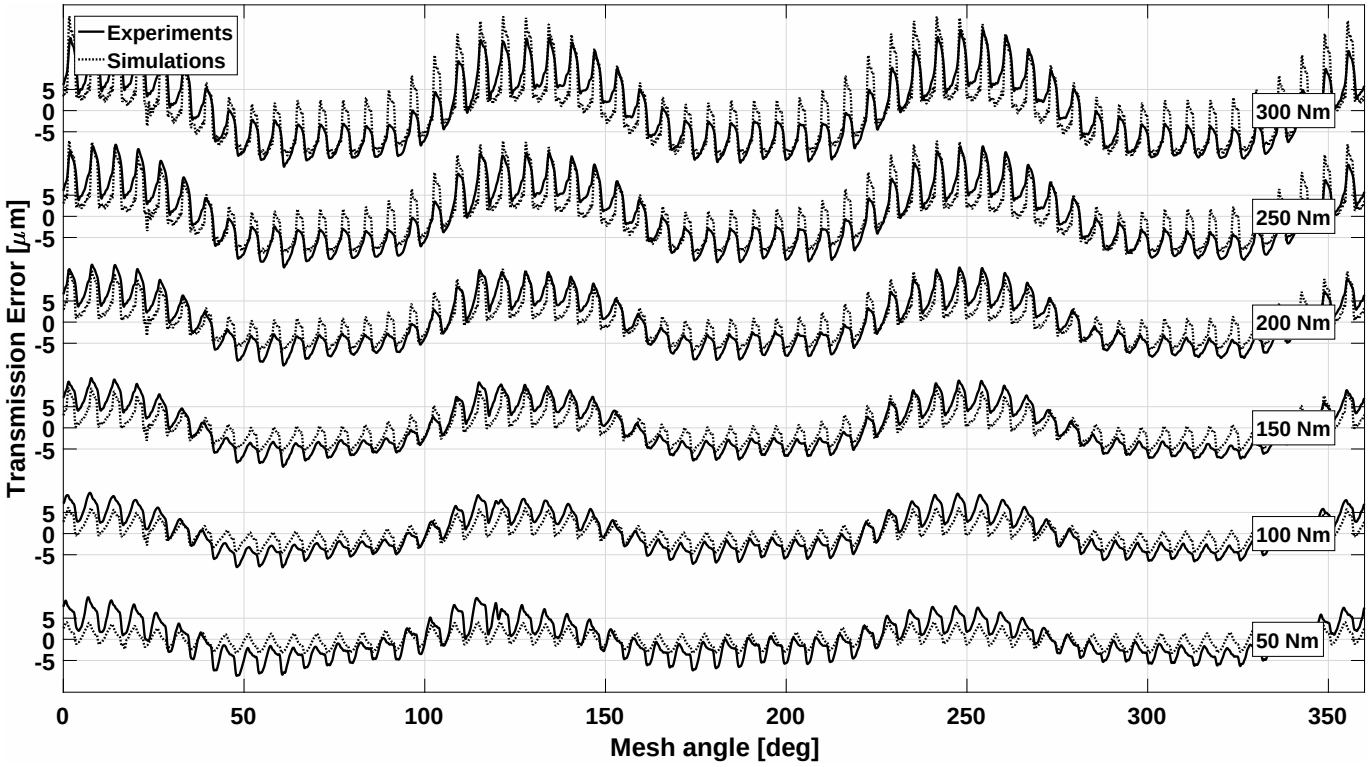

Fig. 9: Transmission error in angle domain for different torque for gear pair B.

The results for gear pair B are reported in figure 9, in the same working conditions as described for gear pair A. In this second case study, the TE curves show a more complex behaviour due to the non-uniform material distribution along the gear body. A low frequency contribution in angular domain is clearly visible in all the curves, with an angular frequency equal to the number of holes present in the lightweight gear, which corresponds to the third order of the gear pair rotation. The level of matching with the experiments is similar to the one obtained for the first case study even if the particular displacement field is more difficult to be captured by the numerical model. The curves corresponding to the higher torques in the result show that the FE-based representation of the body stiffness can model this additional contribution in an accurate way. Still the coupling with other effects such as microgeometry modifications and Hertzian contact loads are properly represented in the simulation environment.

4.4 Root Strain Validation

In this section, the results in terms of strain at the root of the teeth are presented for the two gear pairs analysed (Gear pair A and B). All of the presented plots in this paper refer to the strain in the direction tangential to the surface of the tooth in that section. This is done in order to properly compare the experimental and the numerical results. The strain gauges are attached to the surface of the tooth and follow the curvature in that specific region, as shown in figure 6. This particular configuration is replicated in the simulation environment by computing the strain tensor for each chosen element, and rotating it in the direction determined by the two external nodes of the same element edge textcolorredon the tooth profile. The considered elements are 8-nodes linear hexahedral elements, so the straight segment connecting the nodes defines the direction tangential to the element surface. Since the present work considered only spur gear pairs, the direction tangential to the element surface was derived by considering the nodal coordinates of one of the two element edges, which lie on a plane perpendicular to the gear axis and belong to the external surface of the FE mesh that approximates the involute shape of the teeth. For illustrative purposes, in figure 10, one of the considered edges is reported for one of the elements included in the contact analysis for a given tooth.

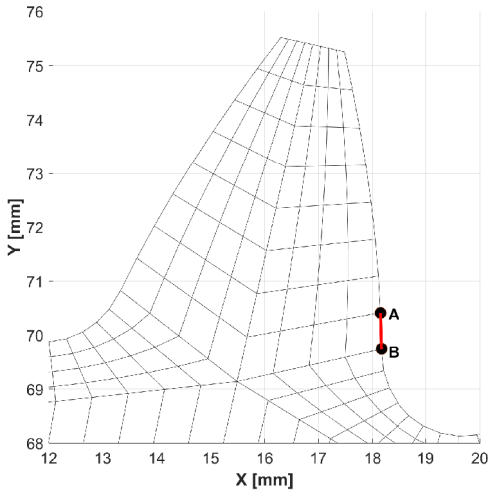

Fig. 10: Representation of the tangential direction to the tooth surface, for a given tooth and element. The nodes A dn B describe the segment that defines the considered direction.

The strain tensor in the global reference frame is therefore rotated according to the local tangential direction at the element surface. The x direction refers to the direction tangential to the element edge and the corresponding component ϵ_x of the strain tensor is considered. Due to the non uniform strain field inside the elements, the choice of the strain computation points reflects the physical gauge location in the selected region of the gear, meaning that the strain field is computed at the centre of the external face of the considered elements on the root fillet. Due to the FE discretization of the gear geometry several elements are present in the analysed portion of the gear, and their dimension is smaller than the selected strain gauges used in the experimental campaign. In such a way, different elements belong to the region covered by a single strain gauge. For this reason an average of the strain values estimated for the different elements is performed, after the strain tensor in each element is rotated in the proper direction.

The gear contact model used in this work allows to recover the displacement field from the global deformation of the gear body, excluding the non-linear displacement field that originates locally in the contact area. Following the analytical description of the contact loads in the method, the inclusion of the local contributions to the displacement in the stress recovery phase is theoretically possible using the well known laws that describe the Hertzian phenomena [36]. The analysis of the tooth root strain involves a region where the distance from the contact zone is sufficiently large to neglect the contribution from the geometrical non-linearities due to the local phenomena, being their extension limited to a small portion of the tooth.

The extension of the load distribution $2L$ due to the local contact deformation, which is the deformation between the tooth surface and the border due to the Hertzian contact pressure, can be calculated using the formula derived by Weber and Banaschek [37]:

$$L = \sqrt{\frac{4}{\pi}((1-\nu_p^2)/E_p + (1-\nu_g^2)/E_g)q\rho} \qquad \rho = \frac{\rho_p \rho_g}{\rho_p + \rho_g} \tag{12}$$

where the load intensity $q = F/b$ is defined as the ratio between the normal load F and the gear thickness b, while ρ is the equivalent radius.

The constants E and ν are respectively the Young modulus and the Poisson ratio of the material and is the width of the gears. The subscripts p and g refer to the pinion and to the gear respectively. According to equations 12, for the gear pairs analysed in this work and with the material and geometrical properties reported in Table 2, the obtained extension of half of the contact area is $L = 0.190$ mm for an applied load of 300 Nm.

	Units	Pinion	Gear
E	[GPa]	210	210
ν	[-]	0.3	0.3
b	[mm]	23	23
ρ	[m]	0.0308	0.0308

Tab. 2: Geometrical characteristics of the analysed teeth

The extent of the contact area is small compared to the tooth dimension and the stress field at the tooth root can be therefore considered as non affected by the Hertzian stress field occurring in the contact region. Its limited extension, indeed, does not generate significant effects in a region distant from the contact forces application point according to the principle of Saint-Venant. In the present work the strain recovery is focused mainly on portions of the gear sufficiently distant from the load application, i.e. the tooth root region.
As explained in section 2 the static modes used for the reduction of the FE stiffness matrix of the gear are computed following the approach originally developed by Vedmar [26].
In order to asses the approximation introduced by using the reduced stiffness matrix $\mathbf{K}_{\text{red}}$ with respect to the full FE stiffness matrix $\mathbf{K}_{\text{FE}}$ on the stress field at the tooth root, the von Mises stress estimated by using both matrices at the centre of some elements belonging to the tooth root region have been compared to each other.

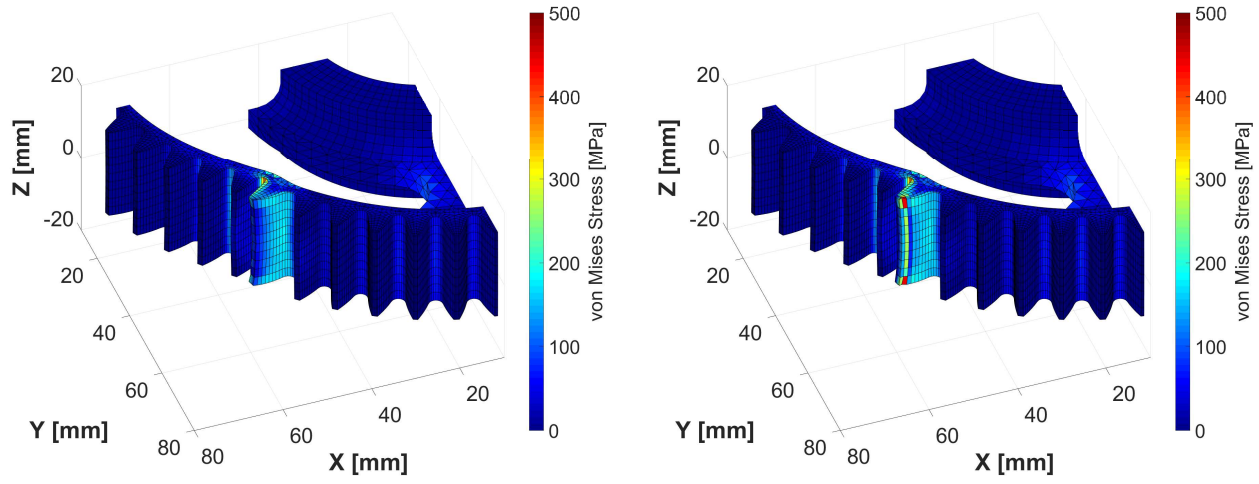

(a) AV modes.

(b) FEM stiffness matrix.

Fig. 11: Detail of the von Mises stress field due to a line load applied on a tooth of a lightweight gear. The colour scale represent the stress value at the centre of the elements (The nodal displacements are magnified 100 times).

The results reported in Table 3 represent the von Mises stresses predicted for three elements along the tooth root for the gear shown in figure 5c, while the von Mises stress field due a line load applied on one tooth of the same gear is shown in figure 11.

Element	**1**	**2**	**3**
$\mathbf{K_{FE}}$	45.9	44.5	38.9
$\mathbf{K_{red}}$	49.0	46.0	40.6
Difference	6.9%	3.2%	4.5%

Tab. 3: Tooth root von Mises element stresses [MPa] using the full stiffness matrix $\mathbf{K}_{\text{FE}}$ obtained from the FE discretisation and the reduced one $\mathbf{K}_{\text{red}}$.

From the numerical results it is possible to conclude that the reduced stiffness matrix approximates the stress field at the tooth root with a maximum error lower than 7%. This observation leds to conclude that the influence due to the reduction of the stiffness matrix is limited.

4.4.1 Friction effects

As explained in section 3, two methods were used in this work to recover the strain due to the meshing loads. The first method is based on a reduced stiffness matrix of the gear trough a series of static modes generated by a normal load with respect to the teeth surface. This means that the reduction space is not rich enough to capture the friction influence and therefore such effects can not be taken into account in the strain recovery phase, but the methodology can be easily extended. In most of the applications where gears rotate at a relatively large rotational speed this does not represent a limitation since the relative speed between the tooth profiles is sufficiently high to generate an appropriate lubrication condition, where the friction coefficient is significantly lower.
In this work low speed analysis were performed, where the rotational speed is not high enough to generate the appropriate lubrication regime. For this reason, the influence of the friction forces on the global deformation of the tooth was investigated. In order to include the friction effects in the analysis, the second approach described in section 3 was used. It is based on the application of the meshing loads, computed during the MB simulation, directly on the full FE mesh of the gear. The meshing loads consist of a normal force vector $\mathbf{F_n}$ which is an output of the dynamic simulation, and a tangential friction force $\mathbf{F_t}$ proportional by the friction coefficient to the amplitude of the normal force, $\mathbf{F_t}=\mu\mathbf{F_n}$.
Since the direction of the friction force is determined according to the direction of the relative velocity between the tooth profiles in the contact point, an additional routine is included in order to properly check when a change of the direction of the relative velocity occurs. Exploiting the kinematic laws of meshing [38], the moment when the friction force changes direction can be individuated in the instant when the contact point crosses the pitch circle.
The influence of a tangential force on the tooth root stress field is analysed quantitatively in an illustrative example. One of the gears examined in this work was loaded with a normal force corresponding to a torque of 250 Nm applied on the nodes at the highest distance from the pitch point, where the friction effects are supposed to have the highest relevance. Two loading scenarios were analysed: in the first scenario, only a normal load was applied, while in the second condition an additional tangential force corresponding to a friction coefficient of 0.3 is applied. The results are reported in terms of von Mises elemental stress computed at the centre of the element for different locations along the tooth root at a given axial position.
By looking at the figure 12, which shows the colour map of the stress distribution on the loaded tooth in the two different load cases, it is evident that the friction is responsible for a reduction of the stress on the loaded flank. Indeed, due to the bending components on the tooth, the flank is loaded with traction stress. On the other hand when the friction is included, it acts as an additional compression component that lowers the stress field generated by the normal force. This consideration is valid when the force application point has a radius which is bigger than the pitch radius. The consideration is exactly the opposite when the radius at the contact point is smaller than the pitch radius. In this case the friction component acts as an additional traction stress field on the tooth root, and therefore increases the stress levels.

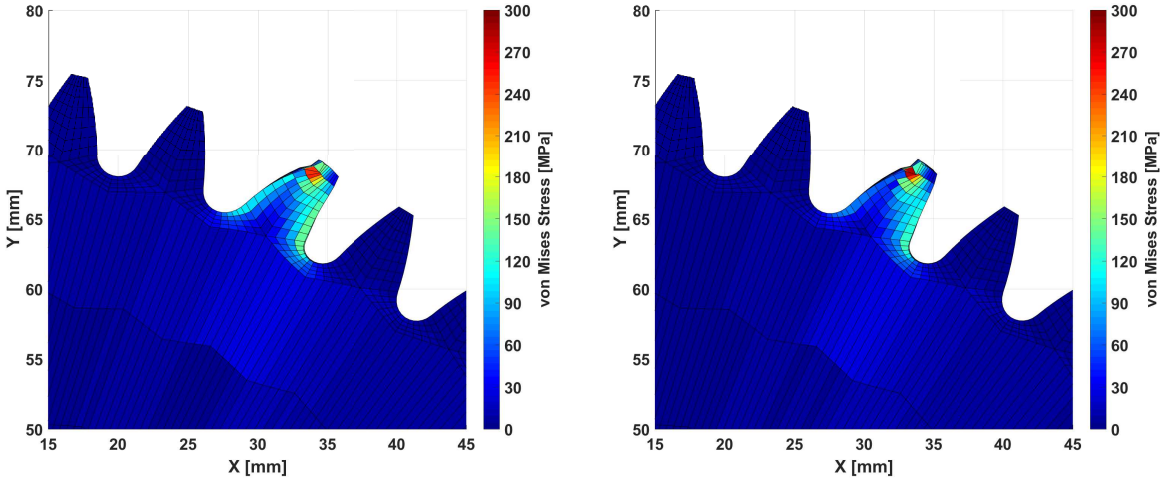

(a) $\mu = 0$

(b) $\mu = 0.3$

Fig. 12: Detail of the von Mises stress field due to a line load applied on a tooth of gear 1. The nodal displacements are magnified 200 times.

The element von Mises stresses reported in Table 4 for the two cases, are compared for five different elements belonging to the root region of the tooth. The difference is up to 38% for the element with the biggest distance from the root among the five analysed. Similar considerations are expected when the friction force has the opposite direction.

Element	**1**	**2**	**3**	**4**	**5**
$\mu = 0$	64.75	87.83	100.43	98.62	86.97
$\mu = 0.3$	49.01	65.40	73.94	71.99	63.06
Difference	32.12%	34.30%	35.83%	37.00%	37.92%

Tab. 4: Tooth root von Mises element stresses [MPa]

4.4.2 Comparison between numerical results and measurements

In figure 13, the ϵ_x component of the strain tensor is presented over the rotation angle at the tooth root for gear 2 of gear pair A. The numerical results, obtained with an applied torque of 50 Nm for the two methods proposed in this work, are presented together with the corresponding experimental results. For this case, the strain field is well predicted by both methods, showing that the friction effects are small in absolute terms at such a low level of applied load. Moreover, it is pointed out that the frictionless strain curve predicted by the first method (Simulation MPF) is very close to the one estimated by the second method (Simulation K_{FEM}) if the friction coefficient is set to zero.

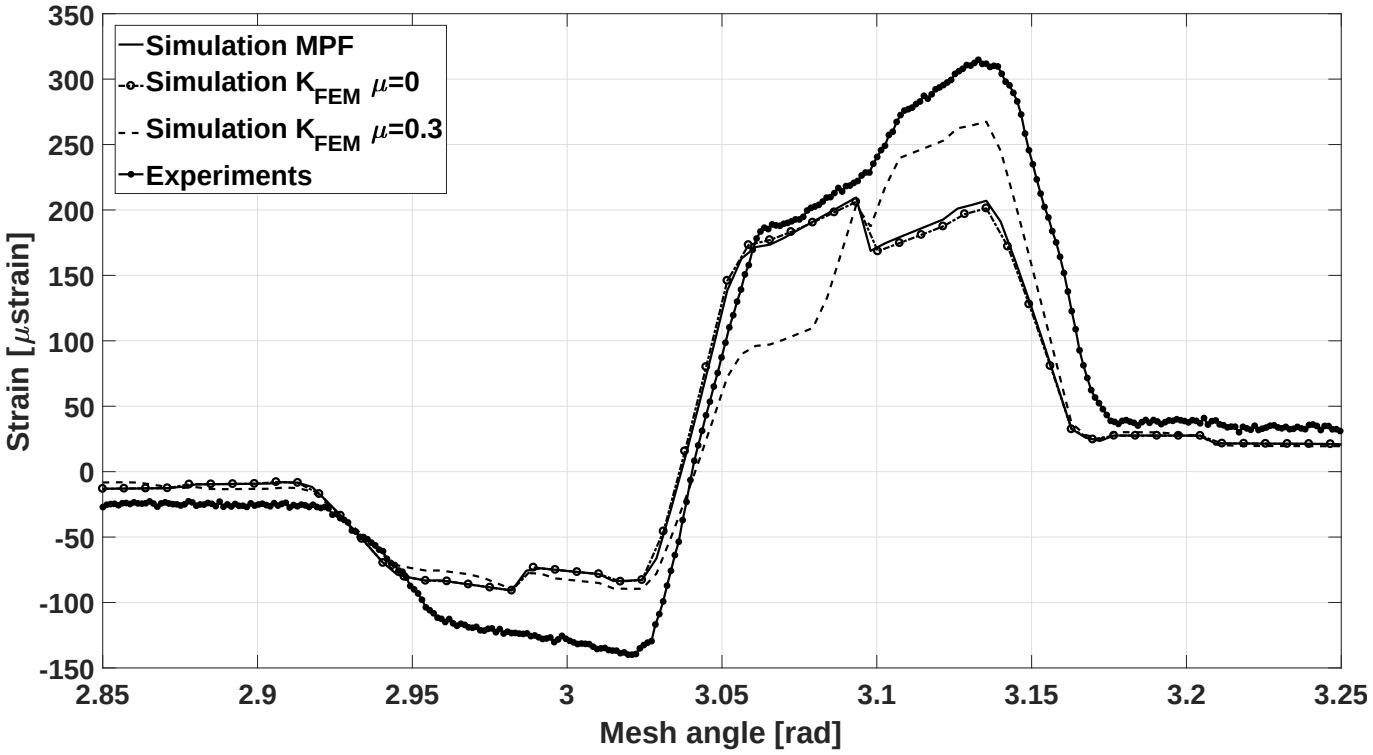

Fig. 13: Root strain versus rotational angle for gear 2 at 50 Nm.

The results shown in figure 14 represent the strain field for a transmitted torque of 300 Nm in the same configuration. As expected, the impact of the friction effects on the predicted strain values is no longer negligible and the global peak to peak amplitude is caught in a more accurate way by the method that takes the friction forces into account. The first method, instead, based on the reduced FE stiffness matrix, shows a good representation of the shape of the curve but it is not capable to show the increase of the strain value due to the additional tangential component of the meshing force.

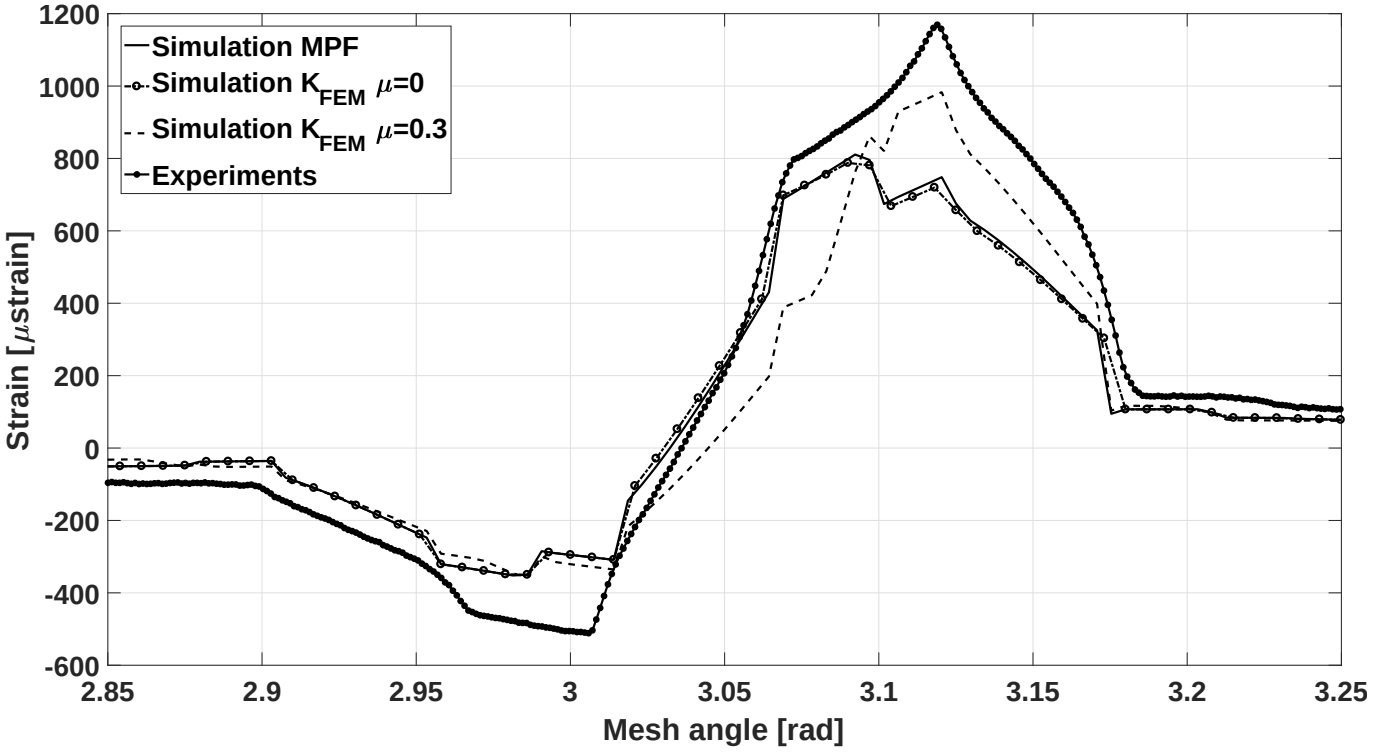

Fig. 14: Root strain versus rotational angle for gear 2 at 300 Nm.

As discussed in the previous section the two methods provide the same strain prediction for a single point corresponding to the instant when the contact point radius coincides with the pitch radius. Under this condition, the sliding speed between the two profiles is equal to zero, meaning that no friction forces are acting on the gears. For all the other points of the predicted strain curves, the two methods provide different results.

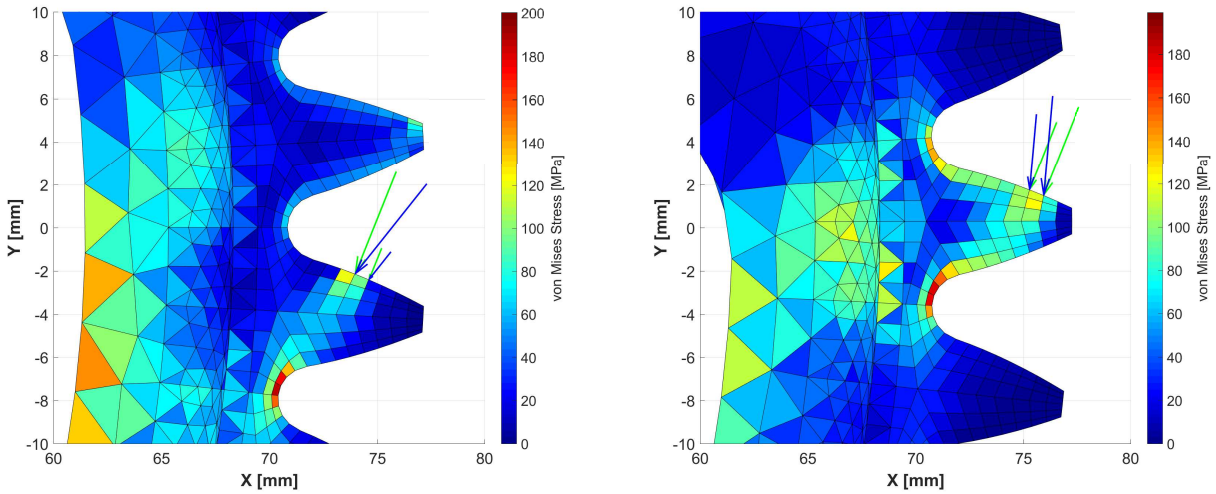

(a) (b)

Fig. 15: Detail of the von Mises stress field with the nodal loads for a given tooth, in two different timesteps. Normal loads are indicated in green, while the nodal loads including friction are represented in blue.

By looking at stress plots in figure 15, where the normal loads acting on the FE mesh are also shown it is possible

to see that for two different meshing positions of the gears, before and after the contact point crosses the pitch circle, the normal nodal load direction (indicated by the green arrows) with respect to the element edges remains constant, neglecting the small displacement of the nodes due to the deformation. In addition, by observing the blue arrows representing the meshing loads including the nodal and the tangential components, it is possible to notice a change in the relative direction with respect to the tooth profile. This change in the direction of the nodal meshing forces causes a sharp change in the strain field in the tooth root.

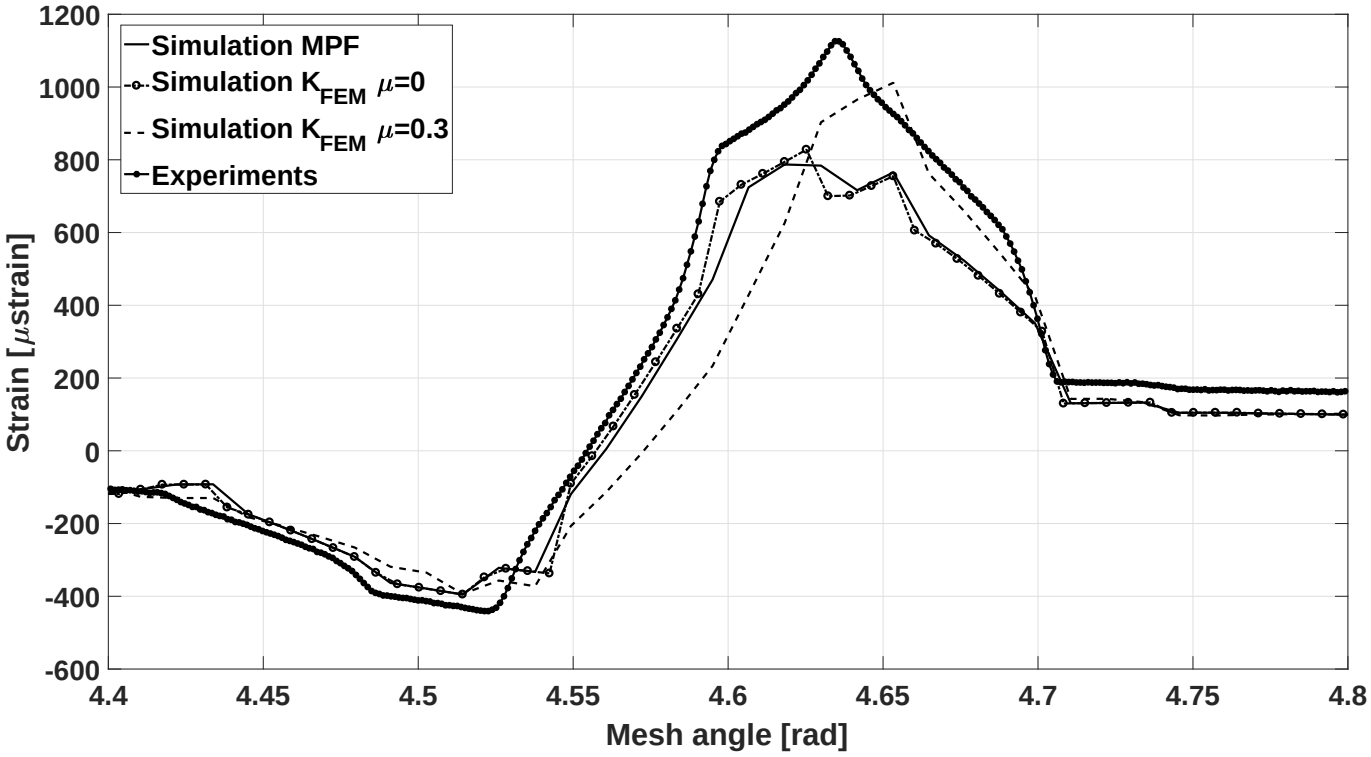

Fig. 16: Root strain over rotational angle for gear 3 at 300 Nm for a tooth close to the bulky region.

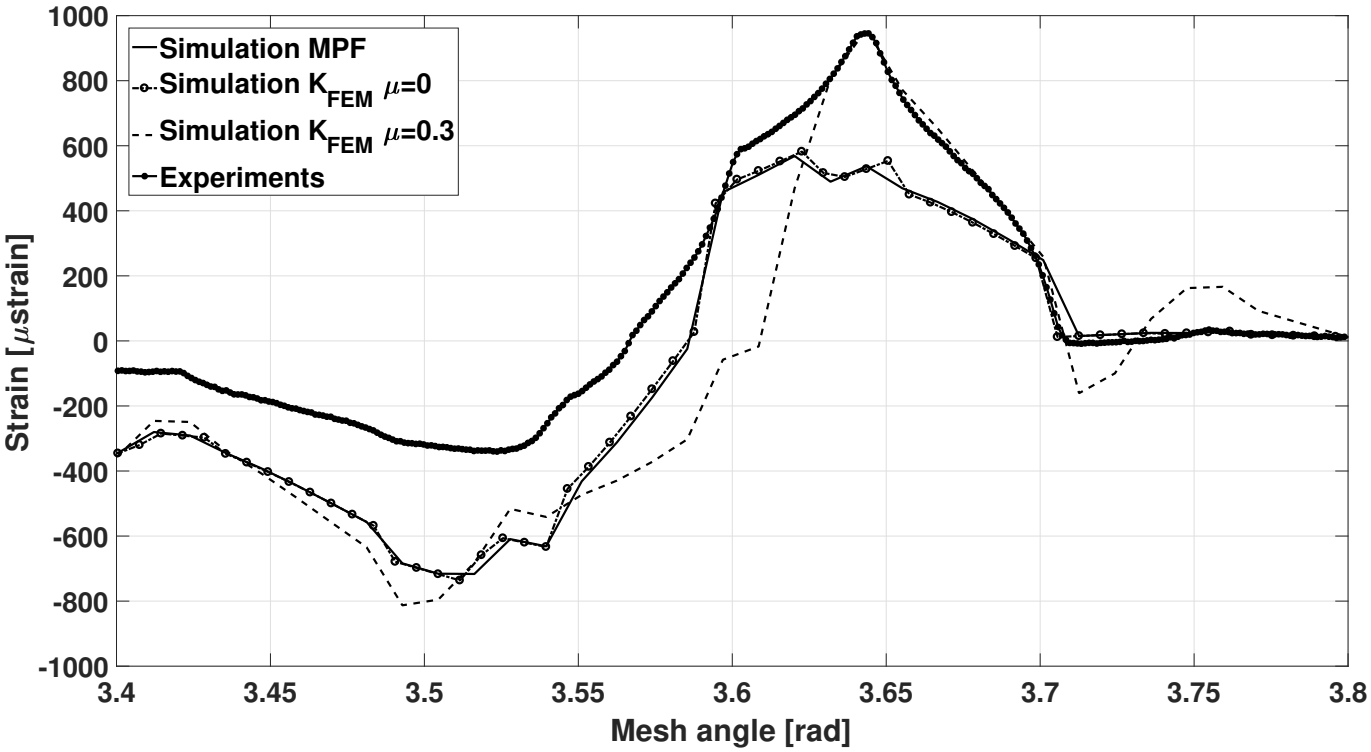

Fig. 17: Root strain over rotational angle for gear 3 at 300 Nm for a tooth close to a slot.

The results for gear 2 of gear pair B are shown in figures 16 and 17 for two different meshing cycles of the gear pair under an applied torque of 300Nm. In figure 16 the root strain curves refer to a meshing tooth close to the bulky portion of the gear body, while in figure 17, the same curves are presented for a meshing tooth close to a slotted region. The shape of the experimental strain curves in angle domain is overall caught by the method.
For all the test cases reported here, the strain curve computed for a friction coefficient equal to 0 using the second method is reported as well. It is possible to notice therefore that when friction is neglected the two methods are equivalent.
Some discrepancies can be observed in the compression region of figure 17, and the phenomena under these effects are under investigation. The fluctuations in the numerical curves visible in picture 17 can be explained by the low level of damping used in the simulation. The effects of system resonances, damping, and interaction with other components will be investigated in future works.
The FE models of gear 2 and gear 3 have 378594 and 245511 DOFs respectively. Their reduced models, instead, consist of 952 and 1380 deformation patterns respectively and each gear is divided into 5 slices, which results in much shorter simulation times for the proposed methodology as compared to full FEM simulations. For instance, assuming that the meshing period is divided into 400 steps, the computation of the strain field for the FE model of gear 2 requires a simulation time of 260 s for the first method and of 650 s using the second method, on an Intel Core i7 @3.5 Ghz computer with 32GB of RAM.

5 Conclusions

in this paper, the application of hybrid analytical-FE approach to solve gear contact problem for detailed multibody analysis in lightweight gears was shown. The method allows to retrieve quantitative results describing the body deformation and stress field with an accuracy similar to non-linear FE methods, but with a much lower computational cost, which allows to simulate long events such as multiple meshing cycles. Moreover, the hybrid formulation offers the possibility to analyse complex systems including lightweight gears with a great level of accuracy. An accurate validation of the method against experimental results shows a very good match of the numerical results in terms of transmission error, even when gears with a particular body topology are analysed. The fidelity of the method in

capturing the displacement of the gear body and the deformation field is also demonstrated by comparison against strain levels measured at the tooth root.
The results illustrated in this paper show a great potential of the method for dynamic system level analysis as well. Future work is planned to validate the purposed method under dynamic conditions.

Acknowledgements

The research leading to these results has received funding from the People Programme (Marie Curie Actions) of the European Union's Seventh Framework Programme FP7/2007-2013/ under REA grant agreement no. 324336 DEMETRA: Design of Mechanical Transmissions: Efficiency, Noise and Durability Optimization.
The research leading to these results has received funding from VLAIO for the project 150394 "ECO-Powertrain"

References

[1] J. M. P. Pérez, F. P. G. Marquez, A. Tobias, and M. Papaelias, "Wind turbine reliability analysis," *Renewable and Sustainable Energy Reviews*, vol. 23, pp. 463 – 472, 2013.

[2] P. Velex and M. Maatar, "A mathematical model for analyzing the influence of shape deviations and mounting errors on gear dynamic behaviour," *Journal of Sound and Vibration*, vol. 191, no. 5, pp. 629 – 660, 1996.

[3] X. Gu and P. Velex, "On the dynamic simulation of eccentricity errors in planetary gears," *Mechanism and Machine Theory*, vol. 61, pp. 14 – 29, 2013.

[4] Y. Chen, Y. Jin, X. Liang, and R. Kang, "Propagation path and failure behavior analysis of cracked gears under different initial angles," *Mechanical Systems and Signal Processing*, vol. 110, pp. 90 – 109, 2018.

[5] S. Park, S. Kim, and J.-H. Choi, "Gear fault diagnosis using transmission error and ensemble empirical mode decomposition," *Mechanical Systems and Signal Processing*, vol. 108, pp. 262 – 275, 2018.

[6] A. F. del Rincon, P. Garcia, A. Diez-Ibarbia, A. de Juan, M. Iglesias, and F. Viadero, "Enhanced model of gear transmission dynamics for condition monitoring applications: Effects of torque, friction and bearing clearance," *Mechanical Systems and Signal Processing*, vol. 85, pp. 445 – 467, 2017.

[7] P. G. Catera, F. Gagliardi, D. Mundo, L. D. Napoli, A. Matveeva, and L. Farkas, "Multi-scale modeling of triaxial braided composites for fe-based modal analysis of hybrid metal-composite gears," *Composite Structures*, vol. 182, pp. 116 – 123, 2017.

[8] S. Shweiki, D. Mundo, and A. Palermo, "A study on the dynamic behaviour of lightweight gears," *Shock and Vibration*, vol. 2017, 2017.

[9] P. Davoli, E. Conrado, and K. Michaelis, "Recognizing gear failures," *Machine Design*, vol. 79, pp. 64–67, 06 2007.

[10] J. A. Korta and D. Mundo, "Multi-objective micro-geometry optimization of gear tooth supported by response surface methodology," *Mechanism and Machine Theory*, vol. 109, pp. 278 – 295, 2017.

[11] T. Lin, H. Ou, and R. Li, "A finite element method for 3d static and dynamic contact/impact analysis of gear drives," *Computer Methods in Applied Mechanics and Engineering*, vol. 196, no. 9, pp. 1716 – 1728, 2007.

[12] P. Ziegler and P. Eberhard, "Simulative and experimental investigation of impacts on gear wheels," *Computer Methods in Applied Mechanics and Engineering*, vol. 197, no. 51, pp. 4653 – 4662, 2008.

[13] S. Vijayakar, "A combined surface integral and finite element solution for a three-dimensional contact problem," *International Journal for Numerical Methods in Engineering*, vol. 31, no. 3, pp. 525–545, 1991.

[14] R. Parker, S. Vijayakar, and T. Imajo, "Non-linear dynamic response of a spur gear pair: Modelling and experimental comparisons," *Journal of Sound and Vibration*, vol. 237, no. 3, pp. 435 – 455, 2000.

[15] R. Parker, A. Vinayak, and S. Vijayakar, "Dynamic response of a planetary gear system using a finite element/contact mechanics model," *Journal of Mechanical Design*, vol. 122, no. 3, pp. 304 – 310, 1999.

[16] X. Dai, C. G. Cooley, and R. Parker, "Dynamic tooth root strains and experimental correlations in spur gear pairs," *Mechanism and Machine Theory*, vol. 101, pp. 60–74, 07 2016.

[17] A. Kahraman, A. Kharazi, and M. Umrani, "A deformable body dynamic analysis of planetary gears with thin rims," *Journal of Sound Vibration*, vol. 262, pp. 752–768, May 2003.

[18] X. Liang, H. Zhang, M. J. Zuo, and Y. Qin, "Three new models for evaluation of standard involute spur gear mesh stiffness," *Mechanical Systems and Signal Processing*, vol. 101, pp. 424 – 434, 2018.

[19] C. Tobias and P. Eberhard, "Stress recovery with krylov-subspaces in reduced elastic multibody systems," *Multibody System Dynamics*, vol. 25, pp. 377–393, Apr 2011.

[20] D. Schurr, P. Holzwarth, and P. Eberhard, "Investigation of dynamic stress recovery in elastic gear simulations using different reduction techniques," *Computational Mechanics*, Nov 2017.

[21] Siemens PLM Software, "Boosting productivity in gearbox engineering." `\protect\unhbox\voidb@x\penalty\@M\https://community.plm.automation.siemens.com/siemensplm/attachments/siemensplm/Simcenter_event_tkb/117/2/Siemens-PLM-Boosting-Productivity-in-Gearbox-Engineering.pdf`, 2017.

[22] P. Wriggers, *Computational Contact Mechanics*. Wiley, 2002.

[23] "ISO 21771. Gears – cylindrical involute gears and gear pairs – concepts and geometry," Intenational Standard, International Organization for Standardization, Geneva, CH, 2007.

[24] "ISO 6336-1. Calculation of load capacity of spur and helical gears — part 1: Basic principles, introduction and general influence factors," Intenational Standard, International Organization for Standardization, Geneva, CH, 2006.

[25] K. G. Murty, F. Yu, and umich edu emurty, "Linear complementarity, linear and nonlinear programming internet edition," 2010.

[26] L. Vedmar, *On the design of external involute gears*. Division of Machine Elements, Department of Mechanical Engineering, Lund Institute of Technology, 1981.

[27] A. Andersson and L. Vedmar, "A dynamic model to determine vibrations in involute helical gears," *Journal of Sound and Vibration*, vol. 260, no. 2, pp. 195 – 212, 2003.

[28] N. Cappellini, T. Tamarozzi, B. Blockmans, J. Fiszer, F. Cosco, and W. Desmet, "Semi-analytic contact technique in a non-linear parametric model order reduction method for gear simulations," *Meccanica – An International Journal of Theoretical and Applied Mechanics*, pp. 1–27, 2017.

[29] C. G. Cooley and R. G. Parker, "Vibration of high-speed rotating rings coupled to space-fixed stiffnesses," *Journal of Sound and Vibration*, vol. 333, no. 12, pp. 2631 – 2648, 2014.

[30] P. Ziegler, P. Eberhard, and B. Schweizer, "Simulation of impacts in geartrains using different approaches," *Archive of Applied Mechanics*, vol. 76, pp. 537–548, Dec 2006.

[31] T. Tamarozzi, G. Heirman, and W. Desmet, "An on-line time dependent parametric model order reduction scheme with focus on dynamic stress recovery," *Computer Methods in Applied Mechanics and Engineering*, vol. 268, pp. 336 – 358, 2014.

[32] B. Blockmans, T. Tamarozzi, F. Naets, and W. Desmet, "A nonlinear parametric model reduction method for efficient gear contact simulations," *International Journal for Numerical Methods in Engineering*, vol. 102, no. 5, pp. 1162–1191, 2015.

[33] D. Malkus, M. Plesha, R. Witt, and R. Cook, *Concepts and Applications of Finite Element Analysis*. Wiley, 2001.

[34] J. D. Smith, *Gear noise and vibration*. Cambridge, 2003.

[35] A. Palermo, L. Britte, K. Janssens, D. Mundo, and W. Desmet, "The measurement of gear transmission error as an nvh indicator: Theoretical discussion and industrial application via low-cost digital encoders to an all-electric vehicle gearbox," *Mechanical Systems and Signal Processing*, vol. 110, pp. 368 – 389, 2018.

[36] K. L. Johnson, *Contact Mechanics*. Cambridge University Press, 1985.

[37] C. Weber, K. Banaschek, and G. Niemann, "Formänderung und profilrücknahme bei gerad-und schrägverzahnten rädern," *F. Vieweg*, 1955.

[38] F. L. Litvin and A. Fuentes, *Gear Geometry and Applied Theory*. Cambridge University Press, 2 ed., 2004.